

Dealloying by peritectic melting

Mingwang Zhong¹ and Alain Karma^{1,*}

¹Physics Department and Center for Interdisciplinary Research in Complex Systems,
Northeastern University, Boston, Massachusetts, 02115, USA

*email: a.karma@northeastern.edu

arXiv:2605.25834v1 [cond-mat.mtrl-sci] 25 May 2026

Abstract

Peritectic melting of Ti–Ag has been shown experimentally to form bicontinuous structures, but the mechanism remains unclear. Here we use phase-field simulations to show that these structures arise from a morphological instability of liquid film migration in three dimensions: a Ti-rich solid growing through an Ag-rich liquid film develops a branched seaweed or dendritic structure whose side branches coalesce to form handles, generating a high-genus bicontinuous topology. A sharp-interface theory predicts a solidification-front velocity and an initial ligament width that are constant in time, in contrast to liquid metal dealloying; subsequent $t^{1/3}$ coarsening reproduces the experimentally observed final ligament width.

Impact statement

Computational modeling reveals the interfacial pattern formation mechanism that transforms a homogeneous peritectic alloy into a two-phase bicontinuous structure by unstable liquid film migration and interface coalescence during the melting process.

Keywords

peritectic melting; dealloying; liquid film migration; bicontinuous structure; phase-field simulation

Introduction

Dealloying is a powerful route for fabricating bicontinuous metals with large interfacial area and useful functional and mechanical properties. These structures enable applications in energy storage^{1,2}, catalysis^{3,4}, sensing^{5,6}, and nanomechanics^{7,8}. Conventional electrochemical dealloying (ECD) selectively dissolves less noble elements from a precursor alloy into an electrolyte^{9–12}, while liquid metal dealloying (LMD) uses a molten metal to dissolve the miscible elements and extends bicontinuous structure formation to systems such as Ta–Ti, Fe–Cr–Ni, and Si–Mg^{13–22}. Vapor phase dealloying (VPD) further exploits vapor pressure differences to selectively remove elements into a vacuum^{23–25}. In all these cases, selective removal or dissolution into an external medium drives the formation of an interconnected solid/liquid or solid/vapor morphology.

Recent experiments have shown that isothermal melting of a peritectic Ti₅₀Ag₅₀ parent β alloy can also generate bicontinuous microstructures^{26,27}. This process differs fundamentally from ECD, LMD,

and VPD because it does not require an external dealloying medium. Upon heating above the peritectic temperature T_p , the metastable β phase decomposes into a Ti-rich α solid and an Ag-rich liquid. Redistribution of Ti and Ag is therefore supported internally by diffusion within the newly formed liquid phase. Among conventional dealloying routes, LMD provides the closest comparison to peritectic melting (PM) because both processes involve two solid phases and a liquid metal. However, in LMD the liquid is an external reservoir, and solute must diffuse through the growing dealloyed layer to the surrounding melt. This produces time-dependent dealloying kinetics, with the dealloying front velocity $v \propto 1/\sqrt{t}$ and the ligament width at the front $\lambda_0 \sim 1/\sqrt{v}$ decreasing and increasing in time, respectively^{15,20}. In PM, by contrast, the liquid forms locally at the melting front, suggesting that the dealloying kinetics may differ from LMD. However, the mechanism by which PM produces a bicontinuous structure and the scaling laws governing v and λ_0 as a function of time and driving force (superheating $\Delta T = T - T_p$) remain unknown.

PM has traditionally been associated with liquid film migration (LFM), in which a thin Ag-rich liquid film advances into the parent β alloy while the α -liquid and β -liquid interfaces migrate in concert^{28,29}. Viewed as a smooth, uniformly advancing front, LFM is topology-preserving and should not by itself generate a high-genus bicontinuous structure. However, recent electron microscopy observations of Ti–Ag peritectic melting suggest that the bicontinuous α/L network develops through LFM²⁷: an α nucleus formed at a premelted β - β grain boundary remains separated from the neighboring β grain by an Ag-rich liquid film and propagates with the receding β -liquid front. This raises the central question: how can LFM, apparently a planar film-migration process, generate high-genus topology?

Here we use phase-field (PF) simulations of PM to answer this question. To isolate the LFM mechanism from the α - β -liquid triple-junction geometry, we initiate growth from a Ti-rich α nucleus fully immersed in the Ag-rich liquid film between neighboring β grains. This avoids imposing uncertain contact angles determined by the interfacial free energies $\gamma_{l\alpha}$, $\gamma_{l\beta}$, and $\gamma_{\alpha\beta}$, which are not accurately known for Ti–Ag, while preserving the essential feature of LFM: two solid-liquid interfaces migrating together across a thin liquid layer. Seeding growth heterogeneously from an α nucleus on a β grain, as observed experimentally^{26,27}, instead of homogeneously inside the inter-grain liquid film yields the same large-scale morphological development of the α -liquid interface. We therefore focus on the homogeneous case, which isolates the mechanism of bicontinuous structure formation from the details of initial nucleus spreading that depend on the triple-junction geometry.

Since crystalline anisotropy is well-known to influence solidification morphologies^{30,31}, we consider both cases where $\gamma_{l\alpha}$ is isotropic and weakly anisotropic. The simulations reveal that, in both two and three dimensions (2D and 3D), the α -liquid interface becomes morphologically unstable forming branched seaweed or dendritic structures with the topology evolving in 3D by coalescence of neighboring branches that form handles and produce a high-genus α/L network. They further show that, in contrast to LMD, v and λ_0 are constant in time, and the structure coarsens behind the front with $\lambda \sim t^{1/3}$ as in Ostwald ripening^{32,33} instead of a smaller coarsening exponent varying between 1/4 and 1/3 due to a mix of surface and bulk diffusion in LMD^{12,20}. We extend existing sharp-interface theories of dendritic solidification^{30,34} and LFM^{29,35,36} to derive the scaling laws $v \sim \Delta T^2$ and $\lambda_0 \sim 1/\Delta T$ that are validated by simulations. These results identify branching and coalescence within morphologically unstable LFM as the mechanism of bicontinuous structure formation, establishing PM as a dealloying pathway distinct from LMD.

Methods

We simulated peritectic melting of Ti–Ag using a multiPF model adapted from a quantitative formulation for eutectic solidification³⁷. The Ag-rich liquid, Ti-rich α solid, and parent β alloy are represented by phase fields ϕ_l , ϕ_α , and ϕ_β , constrained by $\phi_l + \phi_\alpha + \phi_\beta = 1$, together with a conserved Ag concentration field c . The free-energy functional contains gradient, triple-well, and concentration-coupling terms

calibrated to the linearized Ti–Ag phase diagram and to the interfacial free energies $\gamma_{l\alpha}$, $\gamma_{l\beta}$, and $\gamma_{\alpha\beta}$. The phase fields evolve by dissipative relaxation subject to the PF constraint, while c evolves by diffusion with mobility restricted to the liquid phase, so that solute transport vanishes in the solids and reduces to Fickian diffusion in the bulk liquid.

To examine the effect of crystalline anisotropy, the α –liquid interfacial free energy was taken to be either isotropic or weakly anisotropic with cubic symmetry^{30,31}. The equations were solved on a uniform Cartesian grid using second-order central differences and explicit time integration in a CUDA C/C++ implementation. Topological analysis of the dealloyed region was performed by reconstructing the α –liquid interface using marching cubes³⁸; the genus g and ligament size λ were then obtained from the triangulated surface and structure-factor analysis. Full model equations, numerical parameters, calibration details, anisotropy implementation, and topology-analysis procedures are provided in [Supplementary Notes 1–3](#), with parameters listed in [Supplementary Table 1](#)^{39–42}.

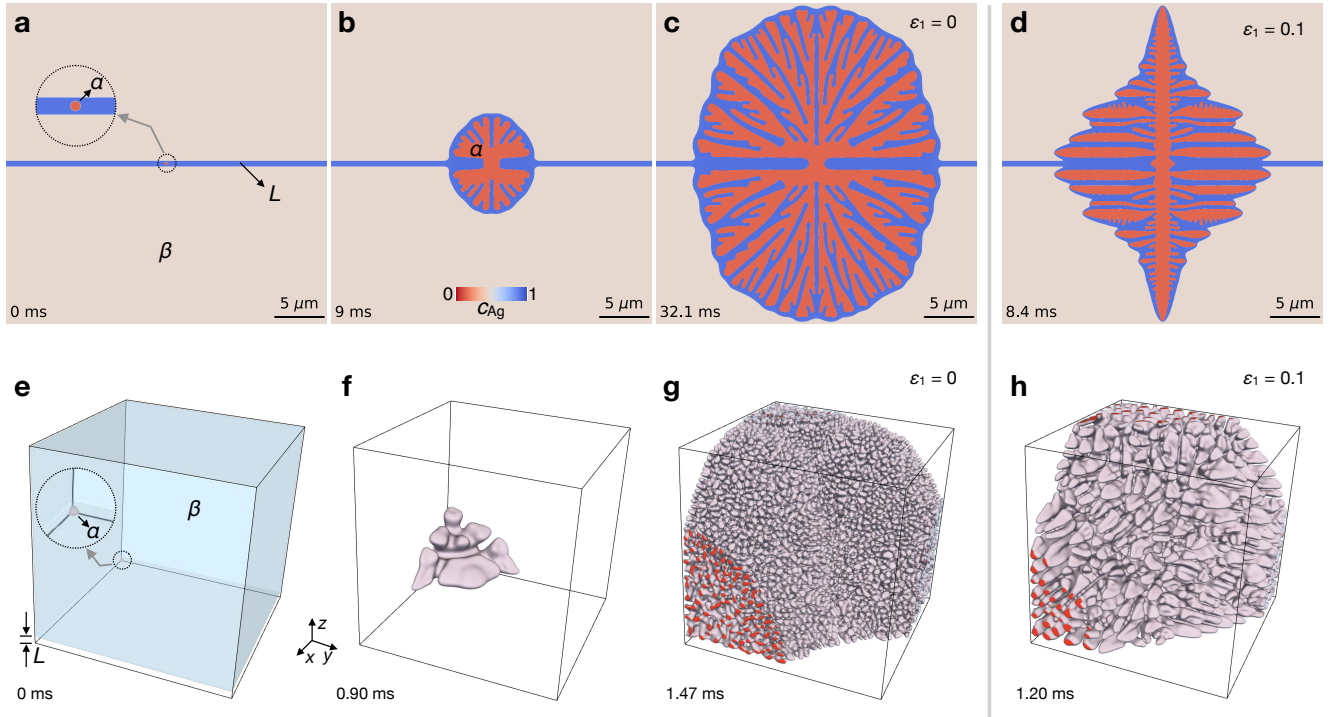


Figure 1: Liquid film migration instability during Ti–Ag peritectic melting. A Ti-rich α nucleus is placed in an Ag-rich liquid film between parent β grains at $\Delta T = 100$ K above the peritectic temperature T_p . (a–c) In 2D with isotropic α –liquid interfacial energy, the advancing interface destabilizes into a seaweed morphology. (d) Fourfold anisotropy selects dendritic branches. (e–g) In 3D, side-branch coalescence converts the unstable front into a bicontinuous α/L network. (h) Fourfold anisotropy biases growth along cubic axes while preserving bicontinuity.

Results and Discussion

Morphological instability of liquid film migration and bicontinuous structure formation

As observed experimentally, melting preceding α nucleation is typically initiated at grain boundaries^{26,27}, consistent with the theoretical expectation that the formation of a liquid film becomes energetically favored at a grain boundary when its excess free-energy $\gamma_{gb} > 2\gamma_{l\beta}$. For this reason, melting is only initiated at a subset of grain boundaries of the initial polycrystalline β microstructure. Since we are

interested in elucidating the topology-generating pattern formation mechanism associated with LFM, we do not model the details of the liquid film formation and α nucleation process. We simply start the simulations from a small initially 2D-circular or 3D-spherical nucleus immersed in a straight liquid film between two β grains. The evolution of such a seed nucleus is shown in Figure 1 in 2D (a-d) and 3D (e-h). In both 2D and 3D, the advancing α -liquid interface destabilizes while remaining separated from the parent β alloy by a continuous liquid film, forming a branched seaweed when $\gamma_{l\alpha}$ is isotropic and a dendritic morphology when $\gamma_{l\alpha}$ is anisotropic.

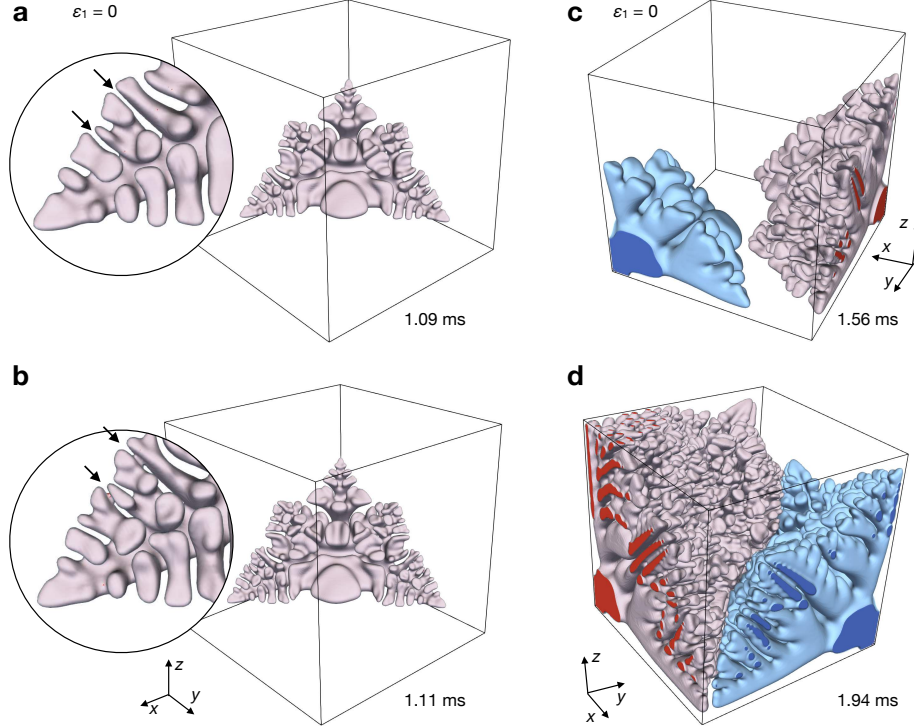


Figure 2: Bicontinuous network formation by side-branch coalescence. 3D phase-field simulations at $\Delta T = 100$ K. (a,b) In a single-nucleus simulation, neighboring α side branches expand laterally and coalesce, closing loops and creating topological handles. (c,d) In a two-nucleus simulation, separate dendritic envelopes coalesce internally and then impinge, producing a polycrystalline bicontinuous network.

These distinct branched morphologies are qualitatively expected from previous studies of single-phase dendritic growth that have highlighted the critical role of crystalline anisotropy in enabling dendritic growth along preferred crystal axes^{30,31}, and the formation of seaweed structures in the absence of anisotropy^{43,44}. However, this role is only secondary here to the formation mechanism of bicontinuous structures, which can be generated in 3D by both seaweed and dendritic growth as illustrated in Figure 1g,h. More important is the topological transformation mediated by the coalescence of neighboring branches that is further illustrated in Figure 2a,b. On the time scale of the simulations of Figure 1d and h, coalescence is only present in the 3D geometry of experimental relevance. This difference can be attributed to the existence of two principal radii of curvature of the α -liquid boundary in 3D, which facilitates transport of excess Ag in the liquid film, enabling α -liquid interfaces to approach closely enough to coalesce in 3D but not in 2D. Each coalescence event closes a loop in the α scaffold and creates a topological handle. Such side-branch coalescence is a known pathway for microstructural connectivity during classical dendritic solidification⁴⁵, but here it occurs within a migrating liquid film and generates bicontinuity during PM. Repetition of this elementary operation across the dealloying front converts a collection of dendritic branches into a connected bicontinuous α /liquid network (Figure 1g). Anisotropy

($\epsilon_1 = 0.1$, Figure 1h) biases growth along the cubic axes but does not suppress branch coalescence, so that the α scaffold remains topologically interconnected.

The same mechanism also explains how polycrystalline bicontinuous structures can form. When two α nuclei with distinct orientations are introduced in the same liquid film, each develops its own dendritic envelope. Branch coalescence first creates connectivity within each envelope, and subsequent impingement produces a polycrystalline bicontinuous network (Figure 2c,d). In this case, the grain scale is set primarily by the initial spacing of α nuclei, while the ligament scale is set by branching and coarsening of the migrating α -liquid interface. PM therefore naturally separates grain-size selection from ligament-size selection, a distinction that may be important for designing polycrystalline bicontinuous microstructures.

Topology and coarsening

To confirm bicontinuity quantitatively, we computed the genus g of the α -liquid interface in cubic sub-volumes of the dealloyed region (Figure 3a). Genus counts independent handles of a closed surface: $g = 0$ corresponds to a sphere-like topology, $g = 1$ to a torus, and $g \gg 1$ to a highly connected network. Details of the marching-cubes reconstruction and genus calculation are given in [Supplementary Note 3](#).

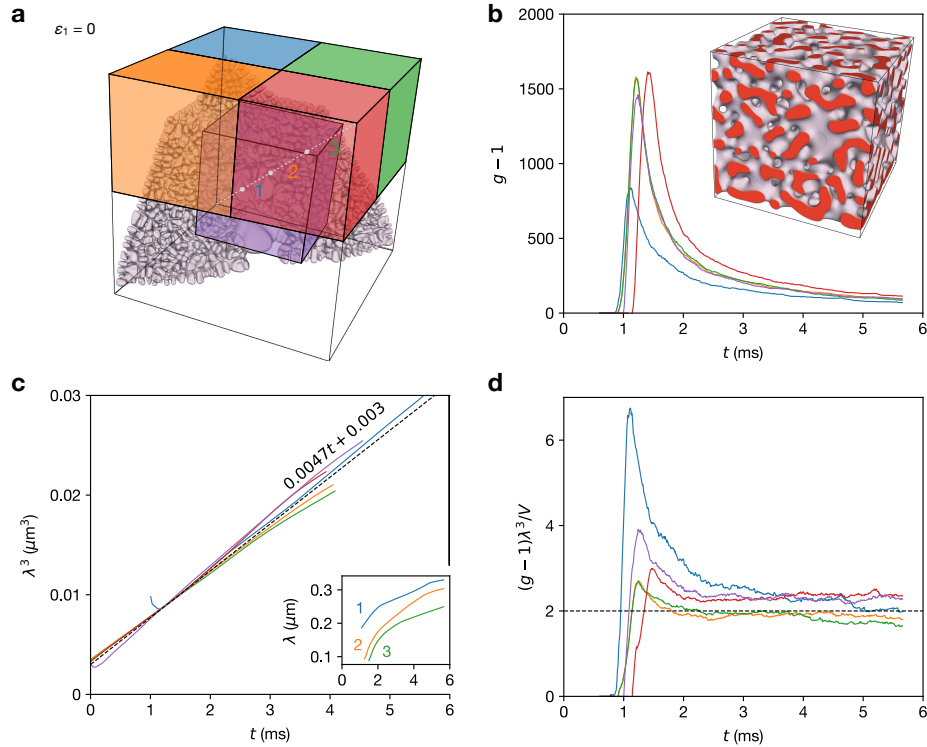


Figure 3: Topology and coarsening of the bicontinuous network. (a) Sub-volumes used to measure the genus g and ligament size λ . (b) Evolution of $g - 1$, confirming a high-genus topology; the inset shows the final morphology. (c) Evolution of the cubed ligament size λ^3 , with curves shifted in time to align local coarsening ages. The inset corresponds to the cube regions marked by diagonal segments 1–3 in panel (a). (d) The scaled genus $(g - 1)\lambda^3/V$, where V is the analyzed volume, approaches ~ 2 .

The genus increases rapidly during the active branching and coalescence stage, reaching values far above unity in all analyzed regions (Figure 3b). This confirms that the α scaffold is not merely branched, but topologically bicontinuous. At later times, g decreases gradually as capillarity-driven coarsening removes small ligaments and eliminates some handles, while remaining well above unity. Thus, the network retains bicontinuity even as its characteristic length scale increases in time.

The ligament size λ , extracted from the structure factor of the α -liquid interface (Supplementary Note 3), follows the Lifshitz–Slyozov–Wagner cubic coarsening law^{32,33}

$$\lambda^3 - \lambda(0)^3 = k(t - t_0), \quad (1)$$

with a fitted coarsening constant $k = 4.7 \mu\text{m}^3/\text{s}$ at superheating $\Delta T = 100 \text{ K}$ (Figure 3c). This value predicts a ligament size of approximately $6.5 \mu\text{m}$ after one minute of dealloying, consistent with experimental observations of Ti–Ag PM^{26,27}. Sub-volumes closer to the initial α nucleus have larger λ at a given time because those ligaments entered the coarsening regime earlier (inset of Figure 3c), providing an internal age gradient within the same simulation.

Combining topology and length scale through the dimensionless quantity $(g - 1)\lambda^3/V$, where V is the analyzed volume, yields a value approaching ~ 2 at long times (Figure 3d). This near-constant scaled genus indicates self-similar coarsening of the bicontinuous structure and is consistent with previous PF studies of nanoporous-metal coarsening⁴⁶. The same behavior is obtained at $\Delta T = 40 \text{ K}$ (Supplementary Figure 2), where $g \gg 1$, λ^3 grows linearly in time, and the scaled genus approaches a similar value, showing that bicontinuity and self-similar coarsening are robust consequences of the LFM instability.

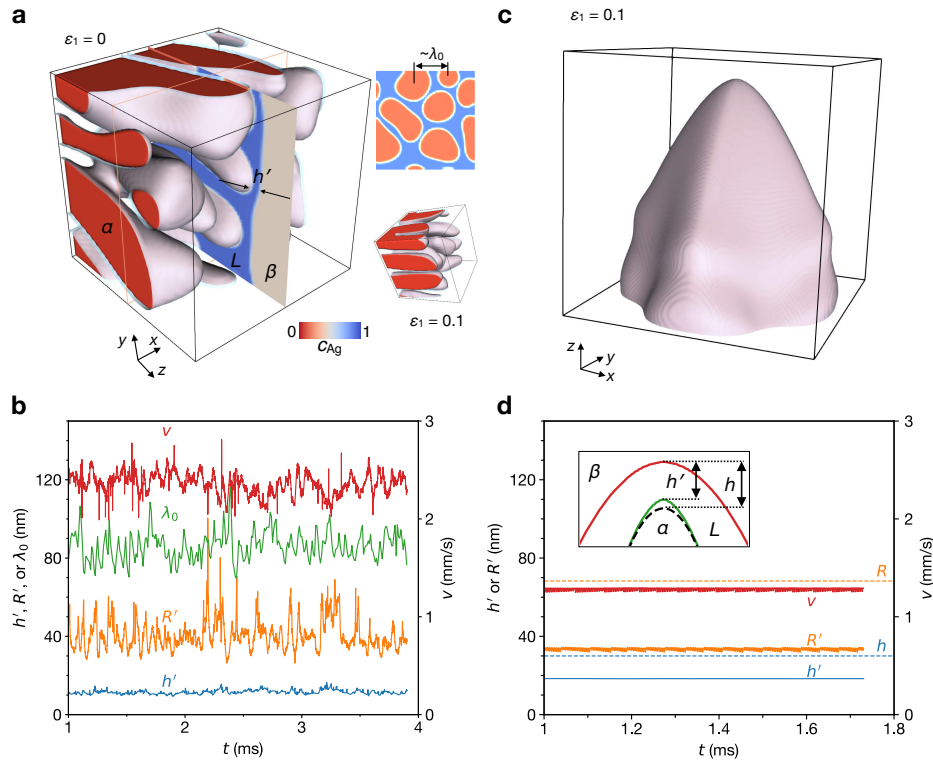


Figure 4: Tip kinetics during peritectic melting. (a) Moving-frame simulation of the multiple-dendrite LFM front. (b) The liquid-film thickness h' , tip radius R' , front-plane ligament size λ_0 , and velocity v remain nearly time-independent. (c) Single-dendrite LFM simulation. (d) In the single-dendrite case, h' and R' are measured directly from the interface, while h and R are obtained from a parabolic fit.

Tip kinetics

A central distinction between PM and conventional LMD lies in the transport geometry. In LMD, the dissolved component must diffuse through the growing dealloyed layer to reach an external liquid medium, which leads to time-dependent kinetics, typically $v \propto 1/\sqrt{t}$ ^{15,20}. In PM, no external reservoir exists. The Ag-rich liquid is generated locally at the melting front, and Ag rejected by the growing α phase is

consumed locally by the receding β -liquid interface. This confines solute redistribution to the migrating liquid film. To investigate the resulting growth kinetics, we performed moving-frame simulations in which the computational domain follows the dealloying front (Figure 4a,b). This geometry allows the front velocity and length scales to be measured over long times. The multiple-dendrite LFM front contains many interacting α fingers, but the averaged quantities are well defined: the liquid-film thickness h' , tip radius R' , front-plane ligament size λ_0 , and growth velocity v all fluctuate around steady mean values. Their approximate time independence is the kinetic signature of local solute redistribution at the PM front and contrasts sharply with the diffusion-limited, time-dependent kinetics of LMD.

Although the multiple-dendrite front forms the bicontinuous network, it is too noisy for direct comparison with a tip-selection theory because individual fingers compete, branch, and coalesce. We therefore isolated the elementary growth unit by simulating a single anisotropy-selected α dendrite advancing through the same liquid-film geometry (Figure 4c,d and Supplementary Figure 3). This reduced configuration assumes that single-dendrite growth kinetics is representative of the average behavior of the multiple-dendrite array, providing a steady LFM tip with well-defined velocity, liquid-film thickness, and curvature that can be directly compared with sharp-interface theory. The fact that isolated dendrites and multiple-dendrite arrays exhibit the same velocity-superheating relationship supports this assumption.

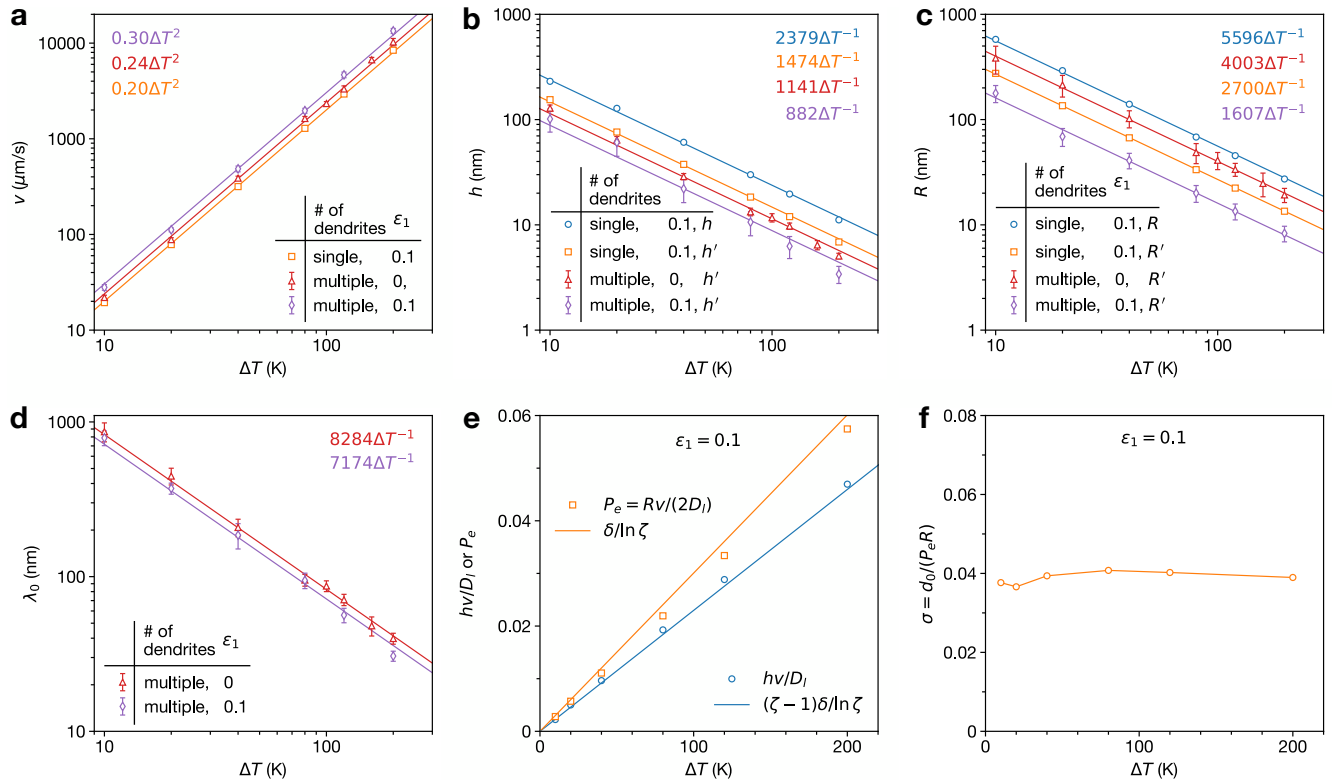


Figure 5: Scaling laws and solvability-type selection. Symbols denote PF measurements for single and multiple dendrites; lines show fits or theoretical predictions. (a) $v \propto \Delta T^2$. (b–d) Film thickness, tip radius, and front-plane ligament size scale as ΔT^{-1} . (e) $h\nu/D_l$ and $Pe = Rv/(2D_l)$ agree with Eq. (2). (f) The stability parameter $\sigma = d_0/(PeR)$ is approximately constant.

The superheating dependence of these kinetic quantities is summarized in Figure 5. For both single- and multiple-dendrite simulations, the growth velocity follows $v \propto \Delta T^2$, while the liquid-film thickness, tip radius, and initial ligament size scale approximately as ΔT^{-1} . The agreement of these scalings across single and multiple (i.e. array of) primary dendrite branches indicates that the bicontinuous front inherits the same tip-scale selection physics branch by branch, even though branch interactions determine the final

network topology. To model the scalings obtained in our PF simulations, we extend the existing sharp-interface theory of dendritic growth^{30,34} to LFM in 3D; previous studies only considered this extension in 2D^{29,35,36} (Supplementary Figure 4). The theory combines two key ingredients: a solution of the diffusion equation in a frame translating at velocity v with mass conservation conditions at the moving α - and β -liquid interfaces assumed to have steady-state parabolic shapes in this frame, which is a direct extension of Ivantsov’s transport theory for a single interface³⁴, and a solvability condition that takes into account the effect of anisotropy³⁰. The diffusion equation solution yields the relations

$$\frac{hv}{D_l} = \frac{(\zeta - 1)\delta}{\ln \zeta}, \quad \text{Pe} = \frac{\delta}{\ln \zeta}, \quad (2)$$

where $\text{Pe} = vR/(2D_l)$ is the Peclet number, which is assumed small, $\text{Pe} \ll 1$, $\delta = (c_{l\alpha} - c_{l\beta})/(c_p - c_{p\alpha})$ is the dimensionless driving force fixed by the superheating ΔT , and $\zeta = (c_p - c_{p\alpha})/(c_p - c_{p\beta})$ is fixed by the Ti–Ag phase diagram. Since $\delta \sim \Delta T$ near T_p , Eq. (2) predicts $hv/D_l \propto \Delta T$ and $\text{Pe} \propto \Delta T$, in agreement with the single-dendrite simulations (Figure 5e). The solvability condition, in turn, predicts that $\sigma = d_0/(\text{Pe}R)$ is a constant determined by the magnitude ϵ_1 of anisotropy, consistent with the nearly constant value of $\sigma \approx 0.04$ extracted from 3D simulations (Figure 5f). These results yield

$$R \propto \frac{d_0}{\sigma\delta}, \quad v \propto \frac{D_l\sigma\delta^2}{d_0}, \quad (3)$$

thereby explaining the observed $R \sim h \sim \Delta T^{-1}$ and $v \sim \Delta T^2$ scalings. Full derivations and definitions of d_0 , δ , and ζ are given in [Supplementary Note 4](#).

Mechanistic implications and outlook

These results establish PM as a self-contained dealloying pathway that is mechanistically distinct from ECD, VPD, and especially LMD. Like LMD, PM involves two solid phases and a liquid metal and produces a high-genus solid/liquid morphology that coarsens self-similarly. Unlike LMD, however, PM requires no external dealloying bath: the liquid is generated internally by decomposition of the peritectic alloy, and Ag redistribution is confined to the migrating liquid film. This local transport explains why the PM front velocity and characteristic length scales remain approximately constant in time, whereas LMD exhibits time-dependent kinetics controlled by long-range diffusion through the dealloyed layer.

PM also provides a natural route to polycrystalline bicontinuous structures. Nucleation at parent β grain boundaries controls the number, spacing, and orientation of α grains, whereas morphological instability of LFM, branch coalescence, and coarsening determine the ligament scale within each grain. This decoupling is absent in many LMD systems (e.g., TaTi dealloyed by a Cu melt¹⁵) where the secondary phase inherits the crystallographic orientation of the precursor alloy (primary phase), and bicontinuous structure formation is mediated by diffusion-limited coupled growth of solid and liquid phases rather than LFM¹⁵. In contrast, in LMD systems where the crystal structures of the primary and secondary phases differ, polycrystalline bicontinuous networks typically form as in $(\text{FeCr})_{70}\text{Ni}_{30}$ dealloyed in liquid Mg⁴⁷ and in SiC dealloyed in liquid Ge¹⁹. In PM, where the parent and product solids are always distinct phases, grain size and ligament size are determined by independent mechanisms, whereas how these scales are selected in the analogous LMD systems remains an open question.

Beyond Ti–Ag, unstable LFM together with interface coalescence may underlie bicontinuous structure formation in other systems with a dealloying medium. For example, the formation of a bicontinuous structure of graphite and a Si-rich phase observed in SiC dealloyed by liquid Ge has been interpreted within the LMD framework¹⁹, but the mechanism has not been explicitly modeled to date. The present results suggest that the formation mechanism may be similar to the one elucidated here since the primary role of Ge is to lower the peritectic transformation temperature of SiC–Ge into graphite and a binary liquid; isothermal melting of SiC (without Ge) would be expected to form bicontinuous structures via

LFM by a similar mechanism as Ti–Ag, albeit at much higher temperature. In this scenario, the presence of a dealloying medium (liquid Ge) would alter the dealloying kinetics with $v \sim 1/\sqrt{t}$ instead of a constant velocity, but topology would be generated by unstable LFM together with interface coalescence instead of unstable two-phase coupled growth¹⁵. The grain size, in turn, would be controlled by nucleation potency independently of the ligament size. The present results enlarge the scope of possible self-organized mechanisms of bicontinuous structure formation during dealloying. Which mechanism is at play in different multicomponent alloy systems remains to be investigated.

Conclusions

Phase-field simulations demonstrate that isothermal melting of an initially homogeneous Ti–Ag peritectic alloy produces a high-genus bicontinuous structure through two sequential mechanisms: a morphological instability of liquid film migration that generates a highly branched structure of the Ti-rich secondary phase, followed by interface coalescence that transforms its topology. The simulations further reveal that the solidification front velocity and the initial ligament width at this front are constant in time, with subsequent coarsening following a $t^{1/3}$ law that predicts a final ligament width in quantitative agreement with experiment. The front velocity and initial ligament width follow scaling laws as functions of superheating in quantitative agreement with sharp-interface theory. These results establish PM as a distinct, internally driven dealloying pathway to bicontinuous structures, with grain size and ligament scale governed by independent mechanisms that can be controlled for microstructure design. More broadly, unstable LFM may underlie bicontinuous structure formation in other alloy systems even in the presence of a dealloying medium and decreasing velocity.

Acknowledgments

This work was funded by the U.S. Department of Energy, Office of Science, Office of Basic Energy Sciences under Award Numbers DE-SC0020895. A.K. wishes to thank Zhongyang Li for valuable discussions. All numerical simulations were carried out on the Explorer cluster of Northeastern University at Massachusetts Green High Performance Computing Center (MGHPCC) in Holyoke, MA.

Declaration of Competing Interests

The authors report there are no competing interests to declare.

Use of AI tools

The authors used Claude Opus 4.7 (Anthropic) in two ways during preparation of this manuscript. First, for copyediting and language refinement of the main text and supplementary notes. Second, for coding assistance with the post-processing scripts used in the topology and structure-factor analyses. The tool was not used to generate scientific content, results, figures, data, or references. After using this tool, the authors reviewed and edited all output and take full responsibility for the integrity, accuracy, and originality of the content of this publication.

References

- [1] Yu-Guo Guo, Jin-Song Hu, and Li-Jun Wan. Nanostructured materials for electrochemical energy conversion and storage devices. *Advanced Materials*, 20(15):2878–2887, 2008.

- [2] Hui Shao, Yih-Chyng Wu, Zifeng Lin, Pierre-Louis Taberna, and Patrice Simon. Nanoporous carbon for electrochemical capacitive energy storage. *Chemical Society Reviews*, 49(10):3005–3039, 2020.
- [3] Volkmar Zielasek, Birte Jürgens, Christian Schulz, Jürgen Biener, Monika M Biener, Alex V Hamza, and Marcus Bäumer. Gold catalysts: nanoporous gold foams. *Angewandte Chemie International Edition*, 45(48):8241–8244, 2006.
- [4] A Wittstock, V Zielasek, J Biener, CM Friend, and M Bäumer. Nanoporous gold catalysts for selective gas-phase oxidative coupling of methanol at low temperature. *Science*, 327(5963):319–322, 2010.
- [5] Kongcheng Hu, Dongxiao Lan, Xuemei Li, and Shusheng Zhang. Electrochemical dna biosensor based on nanoporous gold electrode and multifunctional encoded dna- au bio bar codes. *Analytical chemistry*, 80(23):9124–9130, 2008.
- [6] Jintao Zhang and Chang Ming Li. Nanoporous metals: fabrication strategies and advanced electrochemical applications in catalysis, sensing and energy systems. *Chemical Society Reviews*, 41(21):7016–7031, 2012.
- [7] AM Hodge, J Biener, JR Hayes, PM Bythrow, CA Volkert, and AV Hamza. Scaling equation for yield strength of nanoporous open-cell foams. *Acta Materialia*, 55(4):1343–1349, 2007.
- [8] Hai-Jun Jin, Lilia Kurmanaeva, Jörg Schmauch, Harald Rösner, Yulia Ivanisenko, and Jörg Weissmüller. Deforming nanoporous metal: Role of lattice coherency. *Acta Materialia*, 57(9):2665–2672, 2009.
- [9] Jonah Erlebacher, Michael J Aziz, Alain Karma, Nikolay Dimitrov, and Karl Sieradzki. Evolution of nanoporosity in dealloying. *Nature*, 410(6827):450–453, 2001.
- [10] JR Hayes, AM Hodge, J Biener, AV Hamza, and Karl Sieradzki. Monolithic nanoporous copper by dealloying Mn–Cu. *Journal of Materials Research*, 21(10):2611–2616, 2006.
- [11] J Snyder, T Fujita, MW Chen, and J Erlebacher. Oxygen reduction in nanoporous metal–ionic liquid composite electrocatalysts. *Nature materials*, 9(11):904–907, 2010.
- [12] Ian McCue, Alain Karma, and Jonah Erlebacher. Pattern formation during electrochemical and liquid metal dealloying. *Mrs Bulletin*, 43(1):27–34, 2018.
- [13] John David Harrison and C Wagner. The attack of solid alloys by liquid metals and salt melts. *Acta Metallurgica*, 7(11):722–735, 1959.
- [14] Takeshi Wada, Kunio Yubuta, Akihisa Inoue, and Hidemi Kato. Dealloying by metallic melt. *Materials Letters*, 65(7):1076–1078, 2011.
- [15] Pierre-Antoine Geslin, Ian McCue, Bernard Gaskey, Jonah Erlebacher, and Alain Karma. Topology-generating interfacial pattern formation during liquid metal dealloying. *Nature communications*, 6(1):1–8, 2015.
- [16] Takeshi Wada, Tetsu Ichitsubo, Kunio Yubuta, Haruhiko Segawa, Hirokazu Yoshida, and Hidemi Kato. Bulk-nanoporous-silicon negative electrode with extremely high cyclability for lithium-ion batteries prepared using a top-down process. *Nano letters*, 14(8):4505–4510, 2014.
- [17] Joung Wook Kim, Masashi Tsuda, Takeshi Wada, Kunio Yubuta, Sung Gyoo Kim, and Hidemi Kato. Optimizing niobium dealloying with metallic melt to fabricate porous structure for electrolytic capacitors. *Acta Materialia*, 84:497–505, 2015.

- [18] Ian McCue, Stephen Ryan, Kevin Hemker, Xiandong Xu, Nan Li, Mingwei Chen, and Jonah Erlebacher. Size effects in the mechanical properties of bulk bicontinuous Ta/Cu nanocomposites made by liquid metal dealloying. *Advanced Engineering Materials*, 18(1):46–50, 2016.
- [19] G Greenidge and J Erlebacher. Porous graphite fabricated by liquid metal dealloying of silicon carbide. *Carbon*, 165:45–54, 2020.
- [20] Longhai Lai, Bernard Gaskey, Alyssa Chuang, Jonah Erlebacher, and Alain Karma. Topological control of liquid-metal-dealloyed structures. *Nature Communications*, 13(1):2918, 2022.
- [21] Longhai Lai, Pierre-Antoine Geslin, and Alain Karma. Microstructural pattern formation during liquid metal dealloying: Phase-field simulations and theoretical analyses. *Physical Review Materials*, 6(9):093803, 2022.
- [22] Ruirui Song, Jiuhui Han, Masayuki Okugawa, Rodion Belosludov, Takeshi Wada, Jing Jiang, Daixiu Wei, Akira Kudo, Yuan Tian, Mingwei Chen, et al. Ultrafine nanoporous intermetallic catalysts by high-temperature liquid metal dealloying for electrochemical hydrogen production. *Nature Communications*, 13(1):5157, 2022.
- [23] Zhen Lu, Cheng Li, Jiuhui Han, Fan Zhang, Pan Liu, Hao Wang, Zhili Wang, Chun Cheng, Linghan Chen, Akihiko Hirata, et al. Three-dimensional bicontinuous nanoporous materials by vapor phase dealloying. *Nature communications*, 9(1):1–7, 2018.
- [24] Jiuhui Han, Cheng Li, Zhen Lu, Hao Wang, Zhili Wang, Kentaro Watanabe, and Mingwei Chen. Vapor phase dealloying: A versatile approach for fabricating 3d porous materials. *Acta Materialia*, 163:161–172, 2019.
- [25] Zhen Lu, Fan Zhang, Daixiu Wei, Jiuhui Han, Yanjie Xia, Jing Jiang, Mingwang Zhong, Akihiko Hirata, Kentaro Watanabe, Alain Karma, et al. Vapor phase dealloying kinetics of mnzn alloys. *Acta Materialia*, 212:116916, 2021.
- [26] Wen-Kai Hu, Jun-Chao Shao, Shao-Gang Wang, and Hai-Jun Jin. Evolution of a bicontinuous structure in peritectic melting: The simplest form of dealloying. *Physical Review Materials*, 3(11):113601, 2019.
- [27] Zhongyang Li, Lukas Lühns, Tobias Krekeler, and Jörg Weissmüller. How peritectic melting forms bicontinuous microstructures. *Acta Materialia*, 289:120917, 2025.
- [28] T Muschik, WA Kaysser, and T Hehenkamp. Melting of Cu–In solid solutions at small superheating by droplet formation and liquid film migration. *Acta Metallurgica*, 37(2):603–613, 1989.
- [29] G Boussinot, EA Brener, and DE Temkin. Kinetics of isothermal phase transformations above and below the peritectic temperature: Phase-field simulations. *Acta materialia*, 58(5):1750–1760, 2010.
- [30] A Barbieri and JS Langer. Predictions of dendritic growth rates in the linearized solvability theory. *Physical Review A*, 39(10):5314, 1989.
- [31] Tomorr Haxhimali, Alain Karma, Frédéric Gonzales, and Michel Rappaz. Orientation selection in dendritic evolution. *Nature materials*, 5(8):660–664, 2006.
- [32] Ilya M Lifshitz and Vitaly V Slyozov. The kinetics of precipitation from supersaturated solid solutions. *Journal of physics and chemistry of solids*, 19(1-2):35–50, 1961.
- [33] C Wagner. Theory of the aging of precipitates by dissolution-reprecipitation (ostwald ripening). *Z Elektrochem*, 65(7):581–11, 1961.

- [34] GP Ivantsov. The temperature field around a spherical, cylindrical, or pointed crystal growing in a cooling solution. In *Dokl. Akad. Nauk SSSR*, volume 58, pages 567–569, 1947.
- [35] Efim A Brener and DE Temkin. Velocity-selection problem for combined motion of melting and solidification fronts. *Physical review letters*, 94(18):184501, 2005.
- [36] Efim A Brener and DE Temkin. Melting of alloys along the inter-phase boundaries in eutectic and peritectic systems. *Acta materialia*, 55(8):2785–2789, 2007.
- [37] R Folch and M Plapp. Quantitative phase-field modeling of two-phase growth. *Physical Review E*, 72(1):011602, 2005.
- [38] William E Lorensen and Harvey E Cline. Marching cubes: A high resolution 3d surface construction algorithm. In *Seminal graphics: pioneering efforts that shaped the field*, pages 347–353. 1998.
- [39] Alan T Dinsdale. SGTE data for pure elements. *CALPHAD*, 15(4):317–425, 1991.
- [40] Mei Li, Changrong Li, Fuming Wang, and Weijing Zhang. Experimental study and thermodynamic assessment of the Ag–Ti system. *CALPHAD*, 29(4):269–275, 2005.
- [41] Mingwang Zhong, Adriana Eres-Castellanos, Kaihua Ji, Alec I Saville, Brian Rodgers, Dan R Coughlin, John W Gibbs, John D Roehling, Joseph T McKeown, Amy J Clarke, et al. Quantification and prediction of solidification textures under additive manufacturing conditions. *Nature Communications*, 2025.
- [42] Damien Tournet and Alain Karma. Growth competition of columnar dendritic grains: A phase-field study. *Acta Materialia*, 82:64–83, 2015.
- [43] T Ihle and H Müller-Krumbhaar. Fractal and compact growth morphologies in phase transitions with diffusion transport. *Physical Review E*, 49(4):2972, 1994.
- [44] Silvère Akamatsu, Gabriel Faivre, and Thomas Ihle. Symmetry-broken double fingers and seaweed patterns in thin-film directional solidification of a nonfaceted cubic crystal. *Physical Review E*, 51(5):4751, 1995.
- [45] Nathalie Limodin, Luc Salvo, Elodie Boller, Michel Suéry, M Felberbaum, Sylvain Gaillière, and Kamel Madi. In situ and real-time 3-d microtomography investigation of dendritic solidification in an al–10 wt.% cu alloy. *Acta Materialia*, 57(7):2300–2310, 2009.
- [46] Pierre-Antoine Geslin, Mickael Buchet, Takeshi Wada, and Hidemi Kato. Phase-field investigation of the coarsening of porous structures by surface diffusion. *Physical Review Materials*, 3(8):083401, 2019.
- [47] Morgane Mokhtari, Christophe Le Boulot, Jérôme Adrien, Anne Bonnin, Wolfgang Ludwig, Pierre-Antoine Geslin, Takeshi Wada, Jannick Duchet-Rumeau, Hidemi Kato, and Eric Maire. In situ observation of liquid metal dealloying and etching of porous fe-cr by x-ray tomography and x-ray diffraction. *Materialia*, 18:101125, 2021.

Supplemental Materials: Dealloying by peritectic melting

Mingwang Zhong¹ and Alain Karma^{1,*}

¹Physics Department and Center for Interdisciplinary Research in Complex Systems,
Northeastern University, Boston, Massachusetts, 02115, USA

*email: a.karma@northeastern.edu

Contents

Supplementary Note 1: Phase-field modeling of peritectic melting	2
Supplementary Note 2: Anisotropic α-liquid interfacial free energy	6
Supplementary Note 3: Calculation of genus and characteristic length	8
Supplementary Note 4: Solvability theory of the coupled moving interfaces	9
Supplementary Note 5: Supplementary Figures	11

Supplementary Note 1: Phase-field modeling of peritectic melting

We use the multi-phase-field model of Folch and Plapp³⁷ adapted to the peritectic decomposition of Ti₅₀Ag₅₀, in which the intermetallic β phase melts above T_p into a Ti-rich solid α and an Ag-rich liquid. The state of the system is described by three non-conserved order parameters ϕ_α , ϕ_β , and ϕ_l representing the local volume fractions of the three phases under the constraint $\phi_\alpha + \phi_\beta + \phi_l = 1$, together with the conserved Ag concentration c . We adopt the index convention $\{\alpha, \beta, l\} \rightarrow \{1, 2, 3\}$ throughout. The free-energy functional is

$$\mathcal{F} = \int_V \left[\sum_i \frac{\sigma}{2} |\nabla \phi_i|^2 + H f_\phi(\vec{\phi}) + X f_c(c, \vec{\phi}) \right] dV, \quad (\text{S1})$$

where σ is the gradient-energy coefficient that fixes the diffuse-interface width $W = \sqrt{\sigma/H}$, and H and X are energy-density scales. The multiwell potential

$$f_\phi = \sum_i \phi_i^2 (1 - \phi_i)^2 + \sum_i a_i \phi_j^2 \phi_k^2 (2\phi_j \phi_k + 3\phi_i + b \phi_i^2) \quad (\text{S2})$$

has minima at the three bulk phases. The coefficient a_i controls the interfacial free energy of the jk interface that does not involve phase i , and b raises the energy barrier at the triple junction, suppressing the spurious emergence of the third phase at any two-phase interface. The chemical free-energy density couples $\vec{\phi}$ to c through

$$f_c = \frac{1}{2} \left[c - \sum_i \hat{A}_i(T) g_i(\vec{\phi}) \right]^2 + \sum_i \hat{B}_i(T) g_i(\vec{\phi}), \quad (\text{S3})$$

with

$$g_i(\vec{\phi}) = \frac{\phi_i}{4} \{ 15(1 - \phi_i) [1 + \phi_i - (\phi_j - \phi_k)^2] + \phi_i(9\phi_i^2 - 5) \} \quad (\text{S4})$$

the lowest-order interpolation function that is antisymmetric about $\phi_i = 1/2$ and satisfies $g_i(\phi_i = 0) = 0$, $g_i(\phi_i = 1) = 1$. The temperature-dependent coefficients $\hat{A}_i(T)$ and $\hat{B}_i(T)$ are chosen so that Eq. (S3) reproduces the linearized Ti–Ag phase diagram near T_p :

$$\begin{aligned} \hat{A}_l &= A_1, & \hat{B}_l &= B_1(T), \\ \hat{A}_\alpha &= -A_1 - A_2, & \hat{B}_\alpha &= -B_1(T) - B_2(T), \\ \hat{A}_\beta &= -A_1 + A_2, & \hat{B}_\beta &= -B_1(T) + B_2(T), \end{aligned} \quad (\text{S5})$$

with

$$\begin{aligned} A_1 &= \frac{1}{4}(1 + r), & A_2 &= \frac{1}{2}(1 - r), \\ B_1 &= B_{11} + B_{12}\tilde{T}, & B_2 &= B_{21} + B_{22}\tilde{T}. \end{aligned} \quad (\text{S6})$$

Here $r = \tilde{c}_p = (c - c_{p\beta})/(c_p - c_{p\alpha})|_{c=c_p}$ is the scaled liquidus concentration at T_p and $\tilde{T} = (T - T_p)/[|m_\alpha|(c_p - c_{p\alpha})]$ is the scaled temperature. The phase-diagram parameters T_p , $c_{p\alpha}$, $c_{p\beta}$, c_p , m_α , and m_β are listed in Supplementary Table 1 and visualized in Supplementary Figure 1.

The conserved field evolves by a Cahn–Hilliard equation,

$$\frac{\partial c}{\partial t} = \nabla \cdot [M(\vec{\phi}) \nabla \mu], \quad M(\vec{\phi}) = \frac{D_l \phi_l}{H}, \quad \mu = \frac{\delta \mathcal{F}}{\delta c}, \quad (\text{S7})$$

in which the atomic mobility vanishes linearly with ϕ_l at the solid–liquid interfaces. The non-conserved phase fields follow a constrained Allen–Cahn equation,

$$\tau(\vec{\phi}) \frac{\partial \phi_i}{\partial t} = -\frac{1}{H} \left(\frac{\delta \mathcal{F}}{\delta \phi_i} - \frac{1}{3} \sum_j \frac{\delta \mathcal{F}}{\delta \phi_j} \right), \quad (\text{S8})$$

in which the second term enforces $\sum_i \phi_i = 1$ and the position-dependent time scale $\tau(\vec{\phi})$ is chosen to eliminate the residual interface-thickness dependence of the simulated kinetics. Setting the effective interface kinetic coefficient at the α -liquid and β -liquid interfaces to zero in the thin-interface limit (Eq. (3.41) of Folch and Plapp³⁷) fixes two interface-specific time scales,

$$\tau_\alpha = 0.7464 \tilde{\lambda} |\hat{A}_l - \hat{A}_\alpha|^2 \frac{W^2}{D_l}, \quad \tau_\beta = 0.7464 \tilde{\lambda} |\hat{A}_l - \hat{A}_\beta|^2 \frac{W^2}{D_l}, \quad (\text{S9})$$

where the numerical prefactor 0.7464 comes from the matched asymptotic analysis of Folch and Plapp³⁷, and we define the average $\bar{\tau} = (\tau_\alpha + \tau_\beta)/2$. To ensure that $\tau(\vec{\phi})$ reduces to τ_α inside the α bulk, τ_β inside the β bulk, and $\bar{\tau}$ inside the liquid, we follow Eq. (3.46) of Folch and Plapp³⁷:

$$\tau(\vec{\phi}) = \begin{cases} \bar{\tau} + \frac{(\tau_\beta - \tau_\alpha)(\phi_\beta - \phi_\alpha)}{2(\phi_\alpha + \phi_\beta)}, & \text{if } \phi_l \neq 1, \\ \bar{\tau}, & \text{if } \phi_l = 1. \end{cases} \quad (\text{S10})$$

Equations (S7) and (S8) are non-dimensionalized using W as the length scale and $\bar{\tau}$ as the time scale, giving $\tilde{x} = x/W$, $\tilde{t} = t/\bar{\tau}$, $\tilde{\nabla} = W\nabla$, $\tilde{\mu} = \mu/H$, $\tilde{\mathcal{F}} = \mathcal{F}/H$, and the dimensionless chemical prefactor $\tilde{\lambda} = X/H$. The dimensionless equations are integrated on a uniform Cartesian grid with second-order central finite differences and explicit Euler time stepping. The time step is bounded by the diffusion stability limit,

$$d\tilde{t} = \frac{0.6 d\tilde{x}^2}{2 d_{\text{dim}} \tilde{D}_l}, \quad \tilde{D}_l \equiv \frac{D_l \bar{\tau}}{W^2}, \quad (\text{S11})$$

where $d_{\text{dim}} = 2$ in 2D and $d_{\text{dim}} = 3$ in 3D arises from the central-difference Laplacian of the explicit scheme, and the prefactor 0.6 is chosen small enough to satisfy stability and large enough to accelerate the simulations. The code is implemented in CUDA C/C++; simulations are carried out on NVIDIA V100 or H200 GPUs.

Supplementary Table 1: Parameters of the phase-field model

Parameter	Description	Value
T_p	Peritectic temperature of the Ti-Ag system	1293 K
$c_{p\alpha}$	Ag composition of the α solidus at peritectic temperature	16.41 at.%
$c_{p\beta}$	Ag composition of the β solid at peritectic temperature	50 at.%
c_p	Ag composition of the liquidus at peritectic temperature	93.95 at.%
m_α	Liquidus slope above peritectic temperature	-40.078 K/at.%
m_β	Liquidus slope below peritectic temperature	-26.187 K/at.%
D_l	Diffusion constant in the liquid	$2 \times 10^{-9} \text{ m}^2/\text{s}$
$\gamma_{\alpha l}$	Interfacial free-energy for the liquid- α interface	0.20 J/m ²
$\gamma_{\beta l}$	Interfacial free-energy for the liquid- β interface	0.19 J/m ²
$\gamma_{\alpha\beta}$	Interfacial free-energy for the α - β interface	0.18 J/m ²

Estimation of model parameters

Interfacial free energies, a_i , and b . For each interface, the dimensionless surface free energy is set by the multiwell coefficient associated with the *third* phase. With $\{\alpha, \beta, l\} \rightarrow \{1, 2, 3\}$, $\gamma_{\beta l}$ is controlled by a_1 , $\gamma_{\alpha l}$ by a_2 , and $\gamma_{\alpha\beta}$ by a_3 , through³⁷

$$\tilde{\gamma}_{jk}(a_i) = \frac{2\sqrt{a_i}(3a_i + 4) + (a_i + 4)(3a_i - 4) \operatorname{arccot}(2/\sqrt{a_i})}{16\sqrt{2} a_i^{3/2}}, \quad \gamma_{jk} = \tilde{\gamma}_{jk} WH. \quad (\text{S12})$$

We use a single set of interfacial free energies throughout, $\gamma_{\beta l} = 0.19$, $\gamma_{\alpha l} = 0.20$, and $\gamma_{\alpha\beta} = 0.18$ J/m², corresponding to $a_1 = 4.54285$, $a_2 = 5.58545$, and $a_3 = 3.55521$, respectively. The triple-junction coefficient is fixed at $b = 80$, large enough to fully suppress the spurious appearance of any third phase at a two-phase interface.

Energy-density scale and $\tilde{\lambda}$. The dimensionless prefactor $\tilde{\lambda} = X/H$ is introduced as the relative weight of chemical and gradient-energy contributions in Eq. (S1). Equivalently, in the scaled variables $\tilde{c} = (c - c_{p\beta})/(c_p - c_{p\alpha})$ and $\tilde{\mu} = \mu/H$, it is the slope of the equilibrium chemical potential with respect to concentration,

$$\tilde{\lambda} = \left. \frac{\partial \tilde{\mu}}{\partial \tilde{c}} \right|_{\text{eq}}. \quad (\text{S13})$$

We calibrate $\tilde{\lambda}$ by matching the latent heat of melting across the α -liquid and β -liquid interfaces at T_p , which we compute in two independent ways and equate.

Route 1 — thermodynamic functions. Equilibrium of phase i and liquid at T_p requires equal molar free energies,

$$G_l^m - G_i^m = 0 = H_l^m - H_i^m - T_p(S_l^m - S_i^m) = L_i^m - T_p \Delta S_i^m, \quad (\text{S14})$$

where $L_i^m = H_l^m - H_i^m$ is the latent heat of melting of phase i . Using the Gibbs–Helmholtz identity $S^m = -\partial G^m/\partial T$,

$$L_i^m = T_p(S_l^m - S_i^m) = T_p \left(\left. \frac{\partial G_l^m}{\partial T} \right|_p - \left. \frac{\partial G_i^m}{\partial T} \right|_p \right), \quad (\text{S15})$$

which, evaluated with the published temperature-dependent free-energy functions $G_l^m(T)$, $G_\alpha^m(T)$, $G_\beta^m(T)$ of the Ti–Ag binary^{39,40}, yields $L_\alpha = 15.9$ kJ/mol and $L_\beta = 28.3$ kJ/mol.

Route 2 — phase-field model. The same latent heat can be obtained from the grand-potential balance across the i -liquid interface implied by Eqs. (S1)–(S3). Defining the molar volume V_m and the equilibrium concentration jump $\Delta c_\alpha = c_p - c_{p\alpha}$, the molar free-energy difference takes the compact form

$$G_l^m - G_i^m = \tilde{\mu}^{li} \Delta c_\alpha (\tilde{c}_l^{li} - \tilde{c}_i^{li}) H V_m, \quad (\text{S16})$$

where \tilde{c}_l^{li} and \tilde{c}_i^{li} are the scaled equilibrium concentrations of the liquid and the i solid across the interface, and $\tilde{\mu}^{li}$ is the scaled equilibrium chemical potential at that interface (we omit V_m in what follows since it cancels with the molar normalization on the left-hand side). Differentiating Eq. (S16) along the equilibrium phase boundary at T_p and using Eq. (S15) gives

$$\begin{aligned} L_i &= T_p \Delta c_\alpha \left. \frac{\partial \tilde{\mu}}{\partial T} \right|_{p,\text{eq}} (\tilde{c}_l^{li} - \tilde{c}_i^{li}) H \\ &= T_p \Delta c_\alpha \left. \frac{\partial \tilde{\mu}}{\partial c} \right|_{p,\text{eq}} \left. \frac{\partial c}{\partial T} \right|_{p,\text{eq}} (\tilde{c}_l^{li} - \tilde{c}_i^{li}) H, \end{aligned}$$

where the second line applies the chain rule. The two factors on the second line are evaluated as follows. Along the linearized liquidus on the i side of T_p , $T = T_p + m_i(c - c_p)$ with slope $m_i < 0$, so

$$\left. \frac{\partial c}{\partial T} \right|_{p,\text{eq}} = \frac{1}{m_i}, \quad \text{i.e.,} \quad \left| \left. \frac{\partial c}{\partial T} \right|_{p,\text{eq}} \right| = \frac{1}{|m_i|}. \quad (\text{S17})$$

For the chemical-potential slope, the definition $\tilde{c} = (c - c_{p\beta})/\Delta c_\alpha$ gives $\partial \tilde{c}/\partial c = 1/\Delta c_\alpha$, so Eq. (S13) implies

$$\left. \frac{\partial \tilde{\mu}}{\partial c} \right|_{p,\text{eq}} = \frac{1}{\Delta c_\alpha} \left. \frac{\partial \tilde{\mu}}{\partial \tilde{c}} \right|_{\text{eq}} = \frac{\tilde{\lambda}}{\Delta c_\alpha}. \quad (\text{S18})$$

Substituting Eqs. (S17) and (S18) into Eq. (S17) and using $\tilde{c}_l^{li} > \tilde{c}_i^{li}$ to keep L_i positive, the Δc_α factors cancel and we arrive at

$$L_i = \frac{T_p \tilde{\lambda}}{|m_i|} (\tilde{c}_l^{li} - \tilde{c}_i^{li}) H. \quad (\text{S19})$$

Equation (S19) provides one equation per interface relating $\tilde{\lambda}$ to the latent heat. Using $L_\alpha = 15.9$ kJ/mol and $L_\beta = 28.3$ kJ/mol from Route 1, the parameters in Supplementary Table 1, and the equilibrium concentrations $\tilde{c}_l^{l\alpha}$, $\tilde{c}_\alpha^{l\alpha}$, $\tilde{c}_l^{l\beta}$, $\tilde{c}_\beta^{l\beta}$ read directly from the Folch–Plapp phase diagram at T_p , Eq. (S19) yields $\tilde{\lambda} \approx 25$ from the α -liquid interface and $\tilde{\lambda} \approx 51$ from the β -liquid interface. As a compromise that resolves both interfaces with a single prefactor and keeps the dimensionless equations well conditioned, we adopt $\tilde{\lambda}_{\text{ref}} = 30$ together with $H_{\text{ref}} = 1.462 \times 10^8$ J/m³ and $W_{\text{ref}} = 2$ nm as a reference parameter set; the product $WH = 0.2924$ J/m² then reproduces the dimensional surface energies quoted above.

Width adaptation across superheatings. Because all dimensional surface energies satisfy $\gamma_{jk} = \tilde{\gamma}_{jk} WH$, the product WH uniquely sets the surface tension: doubling W and halving H leaves γ_{jk} unchanged. The latent heat $L_i \propto \tilde{\lambda} H$ is preserved if $\tilde{\lambda}$ is rescaled inversely with H , i.e. $\tilde{\lambda} \rightarrow \tilde{\lambda}(H_{\text{ref}}/H)$. The simulated physics, including the front velocity v , the liquid-film thickness h , and the tip radius R , is therefore invariant under this coupled rescaling. We exploit this freedom to enlarge W at low driving forces, where the underlying physical length scales are intrinsically larger. For each superheating ΔT we use

$$W(\Delta T) = \frac{200 \text{ K}}{\Delta T} \times 2 \text{ nm} = \frac{400}{\Delta T} \text{ nm}, \quad (\text{S20})$$

which recovers $W = 2$ nm at the reference $\Delta T = 200$ K and grows W as ΔT decreases. This choice maximizes the dimensionless grid spacing and time step (Eq. (S11)) and so accelerates the low- ΔT simulations while leaving h , v , and R unchanged to within numerical tolerance.

Supplementary Note 2: Anisotropic α -liquid interfacial free energy

The dependence of the α -liquid interfacial free energy on the orientation of the local interface normal is incorporated only at the α -liquid interface; the β -liquid and α - β interfaces remain isotropic. The dimensionless anisotropy function takes the standard fourfold cubic-harmonic form^{31,41},

$$a_s(\mathbf{n}) = 1 + \epsilon_1 \left(\sum_{i=x,y,z} n_i'^4 - \frac{3}{5} \right), \quad (\text{S21})$$

where \mathbf{n} is the unit normal to the α -liquid interface in the lab frame and $n_i' = \mathbf{n} \cdot \hat{\mathbf{e}}_i'$ is its projection onto the α crystallographic axis $i' \in \{x', y', z'\}$ specified by the orthonormal unit vectors $\mathbf{x}' = (x_1, x_2, x_3)$, $\mathbf{y}' = (y_1, y_2, y_3)$, and $\mathbf{z}' = (z_1, z_2, z_3)$. We use $\epsilon_1 = 0$ for the isotropic simulations and $\epsilon_1 = 0.1$ for the weakly anisotropic simulations of the main text.

The anisotropic surface free energy modifies the evolution equation for ϕ_α in two ways⁴². First, the characteristic time on the left-hand side of Eq. (S8) acquires the orientation-dependent factor

$$\tau(\vec{\phi}) \partial_t \phi_\alpha \longrightarrow \tau(\vec{\phi}) a_s^2(\mathbf{n}) \partial_t \phi_\alpha. \quad (\text{S22})$$

Second, the Laplacian contribution $\sigma \nabla^2 \phi_\alpha$ arising from the gradient-energy term of the functional derivative $\delta\mathcal{F}/\delta\phi_\alpha$ is replaced by the divergence form

$$\nabla \cdot [a_s^2(\mathbf{n}) \nabla \phi_\alpha] + \sum_{i \in \{x,y,z\}} \partial_i \left[|\nabla \phi_\alpha|^2 a_s(\mathbf{n}) \frac{\partial a_s(\mathbf{n})}{\partial (\partial_i \phi_\alpha)} \right], \quad (\text{S23})$$

which reduces to $\nabla^2 \phi_\alpha$ when $\epsilon_1 = 0$. All other terms in the evolution equations for ϕ_α , ϕ_β , and ϕ_l are unchanged.

Two-dimensional implementation. In 2D, $\mathbf{n} = (\cos \theta, \sin \theta, 0)$ where θ is the angle between \mathbf{n} and the lab x -axis, so that the crystal-frame projections are

$$n_x' = x_1 \cos \theta + x_2 \sin \theta, \quad n_y' = y_1 \cos \theta + y_2 \sin \theta, \quad n_z' = z_1 \cos \theta + z_2 \sin \theta. \quad (\text{S24})$$

Following Turret et al.⁴², the anisotropic operator Eq. (S23) is expanded as

$$\begin{aligned} \nabla \cdot [a_s^2 \nabla \phi_\alpha] + \sum_{i=x,y} \partial_i \left[|\nabla \phi_\alpha|^2 a_s \frac{\partial a_s}{\partial (\partial_i \phi_\alpha)} \right] \\ = a_s^2 \nabla^2 \phi_\alpha + 2a_s a_s' (\partial_x \phi_\alpha \partial_x \theta + \partial_y \phi_\alpha \partial_y \theta) + (\partial_x \phi_\alpha \partial_y \theta - \partial_y \phi_\alpha \partial_x \theta) (a_s a_s'' + (a_s')^2), \end{aligned} \quad (\text{S25})$$

with $a_s' \equiv \partial a_s / \partial \theta$ and $a_s'' \equiv \partial^2 a_s / \partial \theta^2$ obtained by differentiating Eq. (S21) through the chain rule and Eq. (S24):

$$\begin{aligned} \frac{\partial a_s}{\partial \theta} &= 4\epsilon_1 \left(n_x'^3 \frac{\partial n_x'}{\partial \theta} + n_y'^3 \frac{\partial n_y'}{\partial \theta} + n_z'^3 \frac{\partial n_z'}{\partial \theta} \right), \\ \frac{\partial^2 a_s}{\partial \theta^2} &= 4\epsilon_1 \left[3n_x'^2 \left(\frac{\partial n_x'}{\partial \theta} \right)^2 + n_x'^3 \frac{\partial^2 n_x'}{\partial \theta^2} + 3n_y'^2 \left(\frac{\partial n_y'}{\partial \theta} \right)^2 + n_y'^3 \frac{\partial^2 n_y'}{\partial \theta^2} + 3n_z'^2 \left(\frac{\partial n_z'}{\partial \theta} \right)^2 + n_z'^3 \frac{\partial^2 n_z'}{\partial \theta^2} \right], \end{aligned} \quad (\text{S26})$$

where the derivatives $\partial n_i' / \partial \theta$ and $\partial^2 n_i' / \partial \theta^2$ follow directly from Eq. (S24). Because $\theta = \tan^{-1}(\partial_y \phi_\alpha / \partial_x \phi_\alpha)$, its first derivatives are

$$\partial_x \theta = \frac{\partial_{xy} \phi_\alpha \partial_x \phi_\alpha - \partial_y \phi_\alpha \partial_{xx} \phi_\alpha}{|\nabla \phi_\alpha|^2}, \quad \partial_y \theta = \frac{\partial_{yy} \phi_\alpha \partial_x \phi_\alpha - \partial_y \phi_\alpha \partial_{xy} \phi_\alpha}{|\nabla \phi_\alpha|^2}. \quad (\text{S27})$$

Three-dimensional implementation. In 3D we work directly with the components of the gradient. Defining $p = \partial_x \phi_\alpha$, $q = \partial_y \phi_\alpha$, $u = \partial_z \phi_\alpha$, and $r = |\nabla \phi_\alpha|$, the projections become

$$n'_x = \frac{x_1 p + x_2 q + x_3 u}{r}, \quad n'_y = \frac{y_1 p + y_2 q + y_3 u}{r}, \quad n'_z = \frac{z_1 p + z_2 q + z_3 u}{r}, \quad (\text{S28})$$

and their derivatives with respect to the gradient components are

$$\begin{aligned} \partial_p n'_x &= \frac{x_1}{r} - \frac{x_1 p^2 + x_2 p q + x_3 p u}{r^3}, \\ \partial_q n'_x &= \frac{x_2}{r} - \frac{x_1 p q + x_2 q^2 + x_3 q u}{r^3}, \\ \partial_u n'_x &= \frac{x_3}{r} - \frac{x_1 p u + x_2 q u + x_3 u^2}{r^3}, \end{aligned} \quad (\text{S29})$$

with the analogous relations for n'_y and n'_z . The derivatives of a_s with respect to p , q , u then take the form

$$\frac{\partial a_s}{\partial p} = 4\epsilon_1 (n_x'^3 \partial_p n'_x + n_y'^3 \partial_p n'_y + n_z'^3 \partial_p n'_z), \quad (\text{S30})$$

and analogously for $\partial a_s / \partial q$ and $\partial a_s / \partial u$. Substituting into Eq. (S23) gives the two anisotropic contributions

$$\begin{aligned} \nabla \cdot [a_s^2(\mathbf{n}) \nabla \phi_\alpha] + \sum_{i \in \{x,y,z\}} \partial_i \left[|\nabla \phi_\alpha|^2 a_s(\mathbf{n}) \frac{\partial a_s(\mathbf{n})}{\partial (\partial_i \phi_\alpha)} \right] \\ = a_s^2 \nabla^2 \phi_\alpha + 2a_s (\partial_x \phi_\alpha \partial_x a_s + \partial_y \phi_\alpha \partial_y a_s + \partial_z \phi_\alpha \partial_z a_s) + \sum_{q \in \{x,y,z\}} \partial_q t_q, \end{aligned} \quad (\text{S31})$$

where

$$t_x = |\nabla \phi_\alpha|^2 a_s \frac{\partial a_s}{\partial p}, \quad t_y = |\nabla \phi_\alpha|^2 a_s \frac{\partial a_s}{\partial q}, \quad t_z = |\nabla \phi_\alpha|^2 a_s \frac{\partial a_s}{\partial u}. \quad (\text{S32})$$

Numerical strategy. The 3D update is implemented as two CUDA kernels: the first computes the auxiliary fields a_s , t_x , t_y , t_z at every grid point; the second uses these fields to assemble the anisotropic contribution and advance ϕ_α . Boundary conditions are applied to all four auxiliary fields on the faces, edges, and vertices of the simulation domain. This split-kernel scheme avoids redundant computation and is roughly twice as fast as a single-kernel implementation in our tests. Because each α orientation requires its own auxiliary fields, the scheme is memory-intensive for polycrystalline simulations with many orientations; the present simulations use a single α orientation, so memory is not a binding constraint.

Supplementary Note 3: Calculation of genus and characteristic length

The bicontinuous topology of the α/L network is quantified by two complementary measures: the genus g of the α -liquid interface, which counts independent handles, and the characteristic length λ extracted from the structure factor of the phase field, which measures the typical ligament size. We follow the marching-cubes-based methodology used by Geslin et al.⁴⁶, summarized below.

Genus from a triangulated interface. The α -liquid interface is extracted from the order parameter ϕ as the level set $\phi = 0$ using the marching-cubes algorithm³⁸, which yields a closed triangulated surface. For a closed orientable surface composed of N_{blob} disjoint connected components with total genus $g = \sum_i g_i$, the Euler characteristic of the triangulation obeys

$$\chi \equiv N_V - N_E + N_F = 2N_{\text{blob}} - 2g, \quad (\text{S33})$$

where N_V , N_E , and N_F are the numbers of vertices, edges, and faces of the triangulation. Solving for g gives

$$g = \frac{1}{2}(2N_{\text{blob}} + N_E - N_V - N_F). \quad (\text{S34})$$

Marching-cubes implementation. In the marching-cubes scheme, each grid cube is classified by the signs of ϕ at its eight corners, yielding $2^8 = 256$ configurations that map, through a precomputed lookup table, to a fixed set of interior triangles and intersected (“cut”) cube edges. Summing over all cubes i and correcting for sharing between neighboring cubes,

$$N_F = \sum_i N_{\text{tri}}^i, \quad N_E = \frac{3}{2} \sum_i N_{\text{tri}}^i, \quad N_V = \frac{1}{4} \sum_i N_{\text{CutEdge}}^i, \quad (\text{S35})$$

where N_{tri}^i is the number of triangles inside cube i and N_{CutEdge}^i is the number of cube edges that the interface crosses. The factor $3/2$ in N_E reflects that each triangle contributes three edges, each shared between two triangles, and the factor $1/4$ in N_V reflects that each surface vertex is shared by four neighboring cubes. Substituting Eq. (S35) into Eq. (S34) and simplifying gives

$$g = N_{\text{blob}} + \frac{1}{4} \sum_i N_{\text{tri}}^i - \frac{1}{8} \sum_i N_{\text{CutEdge}}^i. \quad (\text{S36})$$

The two cube-level quantities N_{tri}^i and N_{CutEdge}^i are read directly from the 256-entry lookup tables, and N_{blob} is obtained by 26-connectivity component labeling of the α phase.

Characteristic length from the structure factor. The characteristic ligament size λ is extracted from the structure factor of the order parameter⁴⁶,

$$S(\mathbf{k}) = \frac{\sum_{\mathbf{r}} \sum_{\mathbf{r}'} e^{-i\mathbf{k}\cdot\mathbf{r}} [\phi(\mathbf{r} + \mathbf{r}')\phi(\mathbf{r}) - \langle\phi\rangle^2]}{N^2(\langle\phi^2\rangle - \langle\phi\rangle^2)} \quad (\text{S37})$$

where $N = N_x N_y N_z$ is the number of grid points in the analyzed sub-volume and $\langle\cdot\rangle$ denotes the spatial average over that sub-volume. Spherical averaging over directions gives the isotropic spectrum $S(k)$ with $k = |\mathbf{k}|$, and the characteristic wavenumber is defined as the spectrum-weighted mean

$$\bar{k} = \frac{\int k S(k) dk}{\int S(k) dk}, \quad \lambda = \frac{2\pi}{\bar{k}}. \quad (\text{S38})$$

The front-plane ligament size λ_0 is computed analogously, with the averages in Eqs. (S37)–(S38) restricted to a two-dimensional cross section taken at the dealloying front.

Supplementary Note 4: Solvability theory of the coupled moving interfaces

This note derives the closed-form tip-scale relations [Eqs. (2)–(3)] used in the main text and provides the analytical curves plotted in Figure 5 and Supplementary Figure 4. The analysis extends the classical Ivantsov–microsolubility description of free dendritic growth^{30,34} to the LFM geometry of PM, in which an advancing α -liquid interface and a retreating β -liquid interface migrate in concert across a thin Ag-rich liquid film. As in the classical theory, the diffusion field around an assumed paraboloidal α tip sets the product Rv , i.e. the Peclet number $\text{Pe} = Rv/(2D_l)$, together with the film thickness h , while microsolubility fixes the stability constant $\sigma = d_0/(\text{Pe} R)$ and so closes the selection problem for R and v separately. The new ingredient relative to free growth is that the second moving interface imposes a second concentration boundary condition behind the α tip.

Geometry and governing equation. The α -liquid tip is approximated as a paraboloid of curvature radius R advancing along z at constant velocity v , and the β -liquid interface as a confocal paraboloid trailing it. In parabolic coordinates normalized to R and centred on the α tip, both interfaces are level surfaces of η : the α -liquid interface lies at $\eta = 1$ and the β -liquid interface at $\eta = \eta_0 > 1$. In the frame co-moving with the tip, the Ag concentration c satisfies the steady advection–diffusion equation

$$D_l \nabla^2 c + v \partial_z c = 0. \quad (\text{S39})$$

The Gibbs–Thomson condition at each interface,

$$c_{li} = c_p - \frac{T - T_p}{|m_i|} - \frac{\Gamma \kappa}{|m_i|}, \quad i = \alpha, \beta, \quad (\text{S40})$$

defines capillary lengths $d_i = \Gamma/[|m_i|(c_p - c_{p\alpha})]$; for the Ti–Ag parameters in Supplementary Table 1 ($m_\alpha = -4007.8$ K, $m_\beta = -2618.7$ K), $d_\alpha \simeq 3.2 \times 10^{-11}$ m and $d_\beta \simeq 4.9 \times 10^{-11}$ m. For tip radii $R \sim 10\text{--}10^3$ nm, the capillary correction to c_{li} is at most $\sim 10^{-3}$, so we ignore the curvature term when solving for the diffusion field and impose $c|_{\eta=1} = c_{l\alpha}$, $c|_{\eta=\eta_0} = c_{l\beta}$, where $c_{l\alpha}$ and $c_{l\beta}$ are read directly from the linearized Ti–Ag phase diagram at the working temperature $T = T_p + \Delta T$. Mass conservation at each interface reads

$$v_n (c_p - c_{pi}) = -D_l \partial_n c|_{\eta=\eta_i}, \quad \eta_\alpha = 1, \quad \eta_\beta = \eta_0, \quad (\text{S41})$$

where v_n is the local normal velocity. Equations (S39)–(S41) form a closed problem for $c(\eta)$, η_0 , and Pe .

Two-dimensional solution. With $x = R\xi\eta$ and $z = R(\eta^2 - \xi^2)/2$, the scale factors are $h_\xi = h_\eta = R\sqrt{\xi^2 + \eta^2}$. Seeking an Ivantsov-type solution $c = c(\eta)$ reduces Eq. (S39) to

$$\frac{d^2 c}{d\eta^2} + 2 \text{Pe} \eta \frac{dc}{d\eta} = 0, \quad (\text{S42})$$

with general solution

$$c(\eta) = A \operatorname{erf}(\sqrt{\text{Pe}} \eta) + B, \quad (\text{S43})$$

where A and B are fixed by $c(1) = c_{l\alpha}$ and $c(\eta_0) = c_{l\beta}$. Taking the ratio of the two mass balances (Eq. (S41)) at $\eta = 1$ and $\eta = \eta_0$ gives

$$\zeta \equiv \frac{c_p - c_{p\alpha}}{c_p - c_{p\beta}} = \eta_0 e^{\text{Pe}(\eta_0^2 - 1)}. \quad (\text{S44})$$

The PF simulations give $\text{Pe} < 0.03$ over the entire range $\Delta T \leq 200$ K (Supplementary Figure 4e), so $\eta_0 \approx \zeta$. Substituting this back into the α -interface mass balance and expanding $\text{erf}(x) \approx 2x/\sqrt{\pi}$ yields a linear concentration profile in η ³⁵ and the closed-form relations

$$\text{Pe} = \frac{\delta}{2(\zeta - 1)}, \quad h = \frac{1}{2}(\zeta^2 - 1)R, \quad \frac{hv}{D_l} = \frac{1}{2}(\zeta + 1)\delta, \quad (\text{S45})$$

where the dimensionless driving force

$$\delta \equiv \frac{c_{l\alpha} - c_{l\beta}}{c_p - c_{p\alpha}} \quad (\text{S46})$$

is linear in ΔT near T_p and the film thickness follows from $h = R(\eta_0^2 - 1)/2$.

Three-dimensional solution. With $x = R\xi\eta \cos \phi$, $y = R\xi\eta \sin \phi$, and $z = R(\eta^2 - \xi^2)/2$, axisymmetric solutions of Eq. (S39) again reduce to a one-dimensional ordinary differential equation,

$$\frac{1}{\eta} \frac{d}{d\eta} \left(\eta \frac{dc}{d\eta} \right) + 2\text{Pe}\eta \frac{dc}{d\eta} = 0, \quad (\text{S47})$$

with general solution

$$c(\eta) = A E_1(\text{Pe}\eta^2) + B, \quad E_1(z) \equiv \int_z^\infty \frac{e^{-t}}{t} dt. \quad (\text{S48})$$

Imposing the same two interfacial conditions, taking the ratio of mass balances, and using the small-argument expansion $E_1(z) \approx \gamma - \ln z + z + O(z^2)$ give

$$\zeta = \eta_0^2 e^{\text{Pe}(\eta_0^2 - 1)} \approx \eta_0^2, \quad \delta \approx \text{Pe} \ln \zeta, \quad (\text{S49})$$

and hence

$$\text{Pe} = \frac{\delta}{\ln \zeta}, \quad h = \frac{1}{2}(\zeta - 1)R, \quad \frac{hv}{D_l} = \frac{(\zeta - 1)\delta}{\ln \zeta}. \quad (\text{S50})$$

Microsolvability and tip-scale selection. Equations (S45) and (S50) fix the products hv and the Peclet numbers Pe as functions of δ and the phase-diagram constant ζ , but, as in the free-dendrite problem, an additional condition is needed to determine R and v separately. Microsolvability theory³⁰ supplies this through the stability constant

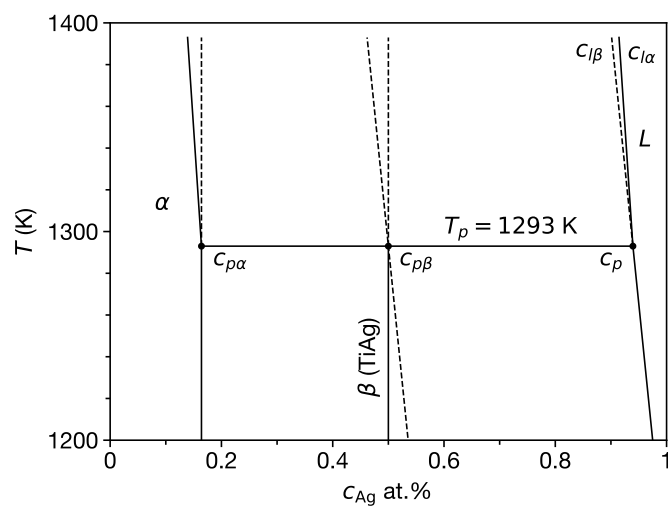
$$\sigma = \frac{d_0}{\text{Pe}R} = \frac{2D_l d_0}{vR^2}, \quad d_0 = \frac{1}{2}(d_\alpha + d_\beta), \quad (\text{S51})$$

which, for given anisotropy strength ϵ_1 of the α -liquid free energy, takes a value independent of δ and hence of ΔT . The PF simulations confirm this prediction: $\sigma \approx 0.04$ in 3D and $\sigma \approx 0.14$ in 2D, both essentially constant over the simulated range $\Delta T \in [20, 200]$ K (Figure 5f and Supplementary Figure 4f). Combining Eq. (S51) with the Ivantsov-type relations yields

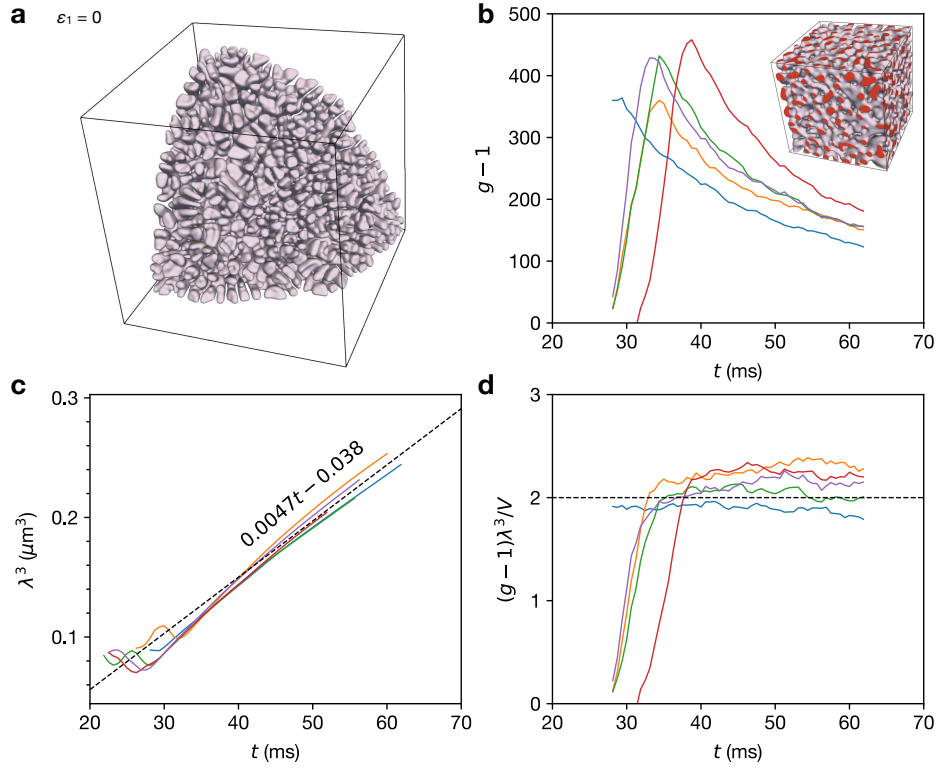
$$R \propto \frac{d_0}{\sigma \delta}, \quad v \propto \frac{D_l \sigma \delta^2}{d_0}, \quad (\text{S52})$$

with ζ -dependent prefactors that differ between 2D and 3D. Since $\delta \propto \Delta T$ near T_p , Eq. (S52) reproduces the observed $R \sim h \sim \lambda_0 \propto \Delta T^{-1}$ and $v \propto \Delta T^2$ scalings of Figure 5a–d and Supplementary Figure 4a–d without adjustable parameters.

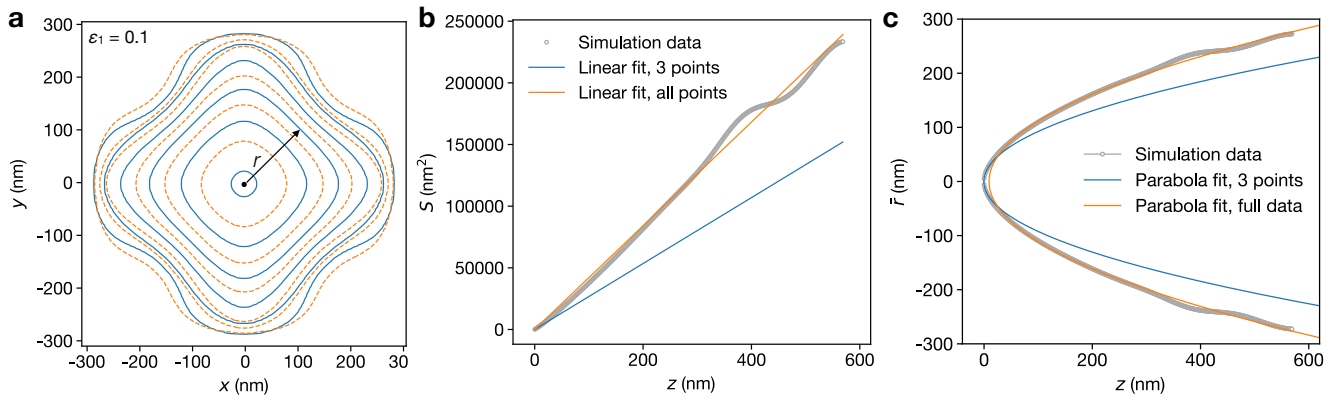
Supplementary Note 5: Supplementary Figures



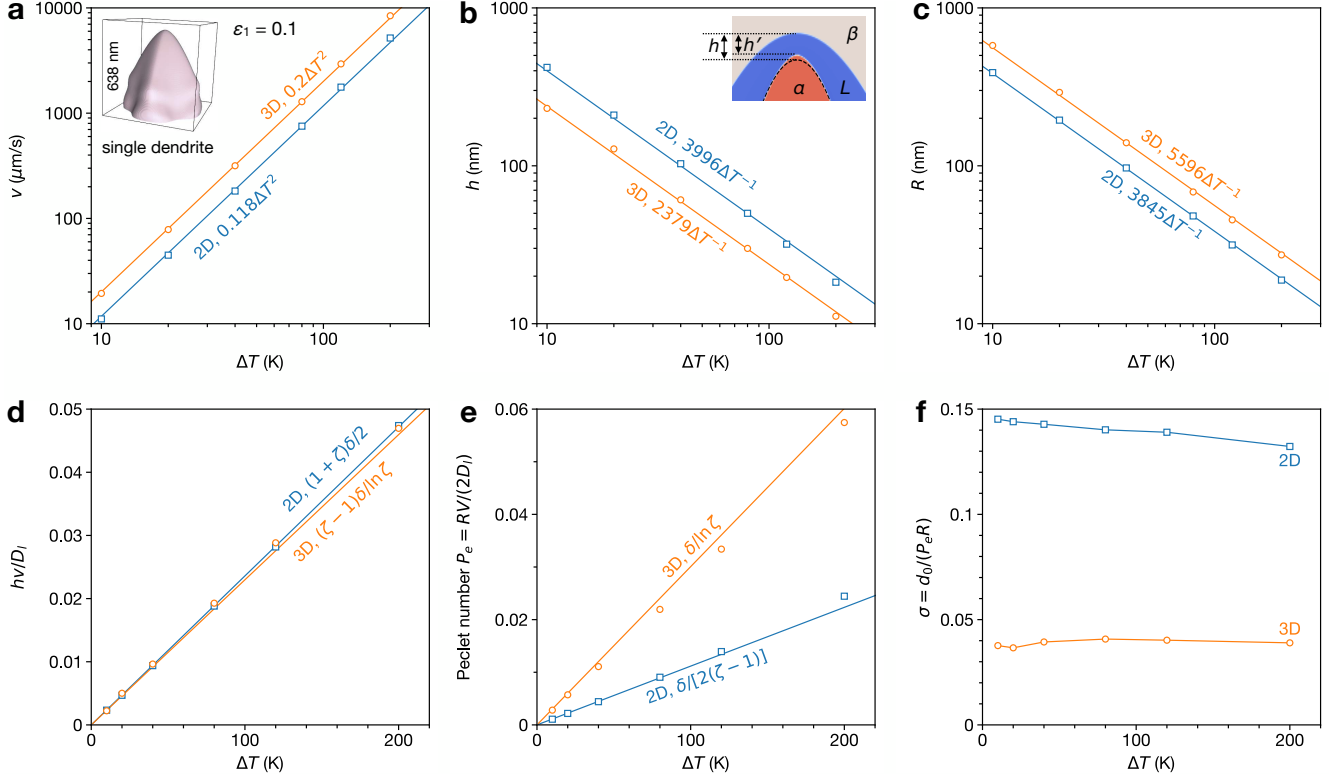
Supplementary Figure 1: Phase diagram of the Ti-Ag system around the peritectic temperature T_p . Parameters are given in Supplementary Table 1.



Supplementary Figure 2: Topology and coarsening of the bicontinuous α /liquid network at $\Delta T = 40$ K. Three-dimensional PF simulation initiated from a Ti-rich α nucleus immersed in the Ag-rich liquid film between neighboring parent β grains; curve colors in (b–d) correspond to the analysis sub-volumes in Figure 3a. **(a)** Hyperbranched α network, with the α -liquid interface shown in brown and the liquid and β phases rendered transparent. **(b)** Evolution of $g - 1$, where g is the genus of the α -liquid interface in each sub-volume. Values $g - 1 \gg 1$ confirm that the dealloyed region is topologically bicontinuous, and the subsequent decrease reflects capillarity-driven coarsening; the inset shows the final α morphology. **(c)** Cube of ligament size, λ^3 , versus time. The curves are shifted in time so as to align λ across sub-volumes. The dashed line is a linear fit, giving $k \simeq 4.7 \mu\text{m}^3/\text{s}$, consistent with the value at $\Delta T = 100$ K (Figure 3c). **(d)** Scaled genus, $(g - 1)\lambda^3/V$, with V the sub-volume, saturating near ~ 2 at long times and indicating robust self-similar coarsening.



Supplementary Figure 3: Parabolic fitting of the α -liquid tip. Analysis of a steady single α dendrite in three dimensions at $\Delta T = 80$ K. **(a)** Contours of the α -liquid interface at distances z behind the tip; r is the in-plane radial distance from the contour center. **(b)** Cross-sectional area S of the α phase versus z . For a paraboloidal tip, $S = 2\pi Rz$, so the slope gives the tip radius of curvature R . **(c)** Mean cross-sectional radius $\bar{r} = (S/\pi)^{1/2}$ versus z , fitted with the parabolic profile using the value of R from (b). The fit determines the parabola-tip position and hence the liquid-film thickness h , measured from this fitted tip to the local β -liquid interface. Fits using only the three points nearest the tip and using all available data give appreciably different values of R and tip position, illustrating the sensitivity of the extracted tip-scale quantities to the fitting range. The fit using all available data is used because it better represents the assumed paraboloidal α -liquid interface.



Supplementary Figure 4: Steady-state tip kinetics in two- and three-dimensional PF simulations. Blue squares and orange circles denote 2D and 3D simulations, respectively, of a single α dendrite growing through the Ag-rich liquid film separating it from the parent β grain. Here, D_l is the liquid diffusivity and d_0 is the capillary length. **(a)** Growth velocity v versus superheating ΔT , showing $v \propto \Delta T^2$ in both dimensions; the inset shows a steady 3D dendrite at $\Delta T = 80$ K. **(b)** Liquid-film thickness h , measured from the fitted parabolic tip to the local β -liquid interface, versus ΔT ; the inset defines h and the directly measured distance h' in 2D. **(c)** Tip radius R obtained from the parabolic fit versus ΔT . Both h and R scale as ΔT^{-1} . **(d)** Dimensionless velocity hv/D_l versus ΔT , compared with the analytical predictions from [Supplementary Note 4](#): $hv/D_l = (1 + \zeta)\delta/2$ in 2D and $hv/D_l = (\zeta - 1)\delta/\ln\zeta$ in 3D, where δ is the driving force and ζ is a phase-diagram constant. **(e)** Peclet number $Pe = Rv/(2D_l)$ versus ΔT , compared with $Pe = \delta/[2(\zeta - 1)]$ in 2D and $Pe = \delta/\ln\zeta$ in 3D. **(f)** Microsolubility stability parameter $\sigma = d_0/(PeR)$ versus ΔT . The nearly constant values, $\sigma \approx 0.14$ in 2D and $\sigma \approx 0.04$ in 3D, are consistent with solvability theory³⁰, where σ is controlled by the interfacial anisotropy; here $\epsilon_1 = 0.1$.